

# Real-time, high-accuracy 3D imaging and shape measurement

Hieu Nguyen,<sup>1,2</sup> Dung Nguyen,<sup>3</sup> Zhaoyang Wang,<sup>1,\*</sup> Hien Kieu,<sup>4</sup> and Minh Le<sup>2</sup>

<sup>1</sup>Department of Mechanical Engineering, The Catholic University of America, Washington, D.C. 20064, USA

<sup>2</sup>Department of Electrical Engineering and Computer Science, The Catholic University of America, Washington, D.C. 20064, USA

<sup>3</sup>Department of Mechanical and Aerospace Engineering, University of California, San Diego, La Jolla, California 92093, USA

<sup>4</sup>Department of Computer Science, Georgia Institute of Technology, Atlanta, Georgia 30332, USA

\*Corresponding author: wangz@cua.edu

Received 2 September 2014; revised 15 October 2014; accepted 15 October 2014;  
posted 16 October 2014 (Doc. ID 222354); published 13 November 2014

In spite of the recent advances in 3D shape measurement and geometry reconstruction, simultaneously achieving fast-speed and high-accuracy performance remains a big challenge in practice. In this paper, a 3D imaging and shape measurement system is presented to tackle such a challenge. The fringe-projection-profilometry-based system employs a number of advanced approaches, such as: composition of phase-shifted fringe patterns, externally triggered synchronization of system components, generalized system setup, ultrafast phase-unwrapping algorithm, flexible system calibration method, robust gamma correction scheme, multithread computation and processing, and graphics-processing-unit-based image display. Experiments have shown that the proposed system can acquire and display high-quality 3D reconstructed images and/or video stream at a speed of 45 frames per second with relative accuracy of 0.04% or at a reduced speed of 22.5 frames per second with enhanced accuracy of 0.01%. The 3D imaging and shape measurement system shows great promise of satisfying the ever-increasing demands of scientific and engineering applications. © 2014 Optical Society of America

*OCIS codes:* (120.2650) Fringe analysis; (150.6910) Three-dimensional sensing; (110.6880) Three-dimensional image acquisition; (120.6660) Surface measurements, roughness; (170.0110) Imaging systems.

<http://dx.doi.org/10.1364/AO.54.0000A9>

## 1. Introduction

In the past two decades, the 3D imaging technologies have drawn considerable interest and gained enormous technical advances. The effects of enhanced 3D imaging performance can be seen in a variety of fields, such as: machine vision, reverse engineering, product inspection, 3D printing, animation production, security monitoring, and unmanned transportation [1–6]. As technologies continue to evolve, there has been a high demand to extend

the capabilities of the 3D imaging techniques to achieve flexible, real-time, fast-speed, high-accuracy, and broad-range performance.

Some commonly used 3D imaging and shape measurement approaches include the stereo vision method, laser scanning method, photogrammetry method, and the structured-light or fringe projection method. It is practically difficult for the former three methods to yield real-time 3D imaging result because of the time-consuming nature of either the stereo matching of correspondent points or the point-by-point scanning operation. In contrast, the technique based on using structured light or fringes, which involves creating and projecting designated

patterns onto the scene and objects, is well known for being capable of achieving real-time imaging performance. Fringe projection profilometry (FPP), also known as the fringe projection technique, is one kind of structured light method and is widely used in numerous applications of 3D imaging and 3D shape measurements [7–15].

Although many FPP-based 3D shape measurement approaches have been developed, there are a few practical challenges restricting the broader applications of the technique. Among these challenges is how to simultaneously possess the capabilities of both fast speed and high accuracy. Zhang and Huang [7] used a modified digital-light-processing (DLP) projector and a fast three-step phase-shifting algorithm to obtain real-time 3D shape measurement at a speed of 40 frames per second (fps); however, the phase unwrapping scheme employed in their work depends on the fact that the phase distributions are continuous over the field of interest, which makes the system inappropriate for applications where isolated regions and/or multiple objects are present. Zuo *et al.* [8] suggested an approach that employs only four projection fringes and a modified DLP projector as well as a field-programmable-gate-array (FPGA) board to reach a speed of 120 fps, but their results have shown relatively low accuracy (a relative error of 0.527%). Meanwhile, Liu *et al.* [9] introduced a dual-frequency and look-up-table (LUT) scheme to obtain real-time measurement at 120 fps, but the DLP discovery kit is prohibitively expensive, and the system is not able to give a reasonably good relative accuracy. It is noted that here the relative accuracy is defined as the ratio of out-of-plane measurement error to the in-plane dimension.

The objective of this paper is to introduce a novel low-cost system that can provide real-time, fast-speed, and high-accuracy 3D imaging and shape measurement. In the proposed system, the imaging accuracy is improved significantly by employing a generalized system setup, multiple-frequency fringe projection approach, hyperaccurate flexible calibration method, and a robust intensity-nonlinearity compensation scheme. A DLP projector is modified and synchronized with a fast-speed camera to yield fast-speed acquisition of images. In addition, owing to the adoption of a graphics processing unit (GPU) and multithread parallel computation, the system can achieve high-speed image and data processing. These allow carrying out 3D imaging and shape measurement with high accuracy at a real-time (or fast-speed) manner. A few experiments have been conducted to demonstrate the validity and practicability of the proposed system, which gives great promise of satisfying the ever-increasing speed and accuracy demands of 3D imaging and shape measurement in scientific and engineering applications.

## 2. Hardware Enhancements

A FPP-based 3D imaging and shape measurement system is typically comprised of a projector, camera,

and a computer. The technique involves projecting a set of fringe patterns onto the objects of interest. The surface height/depth information of the objects is naturally encoded into the distorted fringe patterns. The objects and fringe patterns are then captured by the camera for subsequent 3D point cloud reconstruction. The advantages of the FPP-based 3D imaging and shape measurement can be recognized through the following technical features: (1) full-field imaging, (2) easy implementation, and (3) relatively fast and accurate measurement. To achieve enhanced performance in practice, two kinds of approaches are usually adopted. One approach uses a composite fringe pattern to speed up the projection by taking advantage of the DLP projector, and this can lead to fast-speed 3D shape acquisition with acceptable accuracy. The other approach uses multiple-frequency fringe patterns to obtain very high imaging accuracy with a reduced speed. In regard to the style of the projection fringes, the approach employing sinusoidal fringes and phase shifting scheme is the most widely used technique due to its automatic, full-field, and fast analysis and processing. Therefore, they are employed in this work.

In the proposed system, an external board is introduced into the system. The board serves as a synchronizer for the camera and the projector to substantially boost the imaging speed. Figure 1 illustrates a schematic of the proposed system.

### A. Modified DLP Projector for Pattern Illumination

The single-chip DLP and three-chip liquid-crystal-display (3LCD) are the two primary technologies used in modern color digital projectors. Both technologies have advantages and disadvantages, and at present share the majority of the market. To facilitate the 3D point reconstruction, the proposed system uses three or more phase-shifted fringe patterns to determine the full-field phase distributions. The imaging speed can be significantly increased by using an interesting mechanism of the single-chip DLP projector.

Inside the single-chip DLP projector, there is a color wheel between the lamp and the DLP chip.

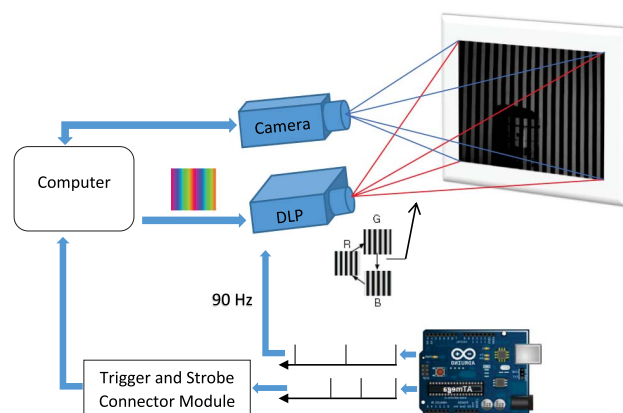


Fig. 1. Schematic of the proposed system.

The color wheel is often divided into multiple sectors, including three in primary colors of red (R), green (G), and blue (B), as well as a transparent colorless sector (clear sector) for enhancing the projection brightness. In some models, a color wheel may also include secondary colors such as cyan, magenta, and yellow. The DLP chip is synchronized by the rotating motion of the color wheel, which allows the color channels of an image or a video frame to be projected sequentially at a sufficiently high rate so that human eyes can see a composite colorful image or video. In the proposed system, a DLP projector with a four-sector color wheel is employed. The timeline for a projection cycle at a frequency of 90 Hz, i.e., each projection cycle lasts for 11.11 ms, is illustrated in Fig. 2.

To take advantage of the above projection mechanism, the color wheel is removed from the DLP projector; this leads to a gray scale image projection for any color image. Meanwhile, a fast speed complementary-metal-oxide-semiconductor (CMOS) camera with a short exposure time (of 3.66 ms in this work) is employed to capture each RGB channel of the image (other non-RGB channels, if existing, can be skipped). Consequently, three different images can be captured in each cycle if they are encoded, respectively, in red, green, and blue channels, and combined into a single source image. Figure 3 is a computer generated source image whose RGB channels are three uniformly-phase-shifted sinusoidal patterns. As a result, the projecting speed virtually becomes three times faster.

#### B. Projecting and Capturing Synchronization with External Triggering Circuit

An external triggering circuit based on a microcontroller Arduino board is employed to control and synchronize the capturing process of the fast speed camera with the projecting process of the DLP projector. In order to trigger the DLP projector externally, the internal triggering circuit, which is

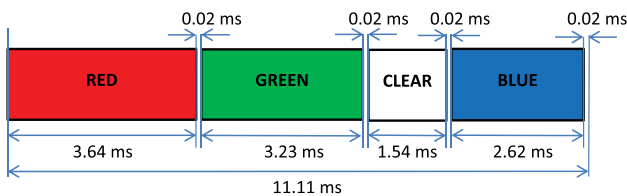


Fig. 2. Timeline for a projection cycle of 90 Hz.

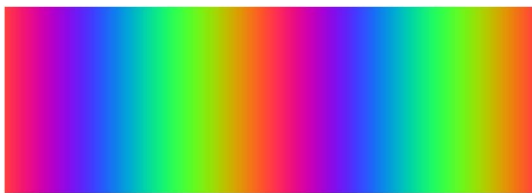


Fig. 3. Composite image of three phase-shifted sinusoidal fringe patterns encoded into RGB channels.

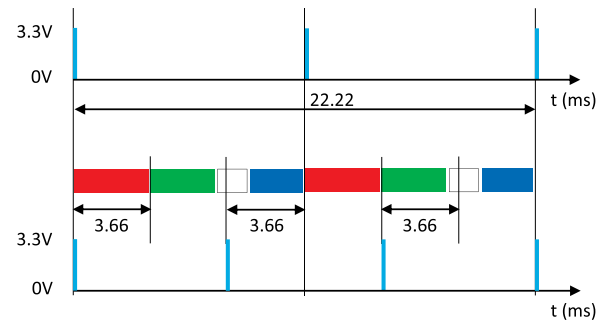


Fig. 4. Synchronization of the projecting and capturing processes.

normally attached to the panel of the color wheel, is removed. After that, two wires, ground and input, are wired out of the projector. The ground wire is then linked with the ground of the Arduino board, whereas the input wire is connected to one output pin of the Arduino board to get the desired control signal. To trigger the camera with the same circuit, a 3.3 V low-voltage transistor-transistor-logic (LVTTL) trigger and strobe connector module is needed. This module will transmit the trigger signal to the computer to control the camera. With this microcontroller, there is no longer a delay for the synchronization between the camera capturing and the projector projecting. As mentioned previously, in the ideal case, three images can be obtained in each projection cycle. In reality, the camera employed in the system has a minimum retrigger period of 5 ms between shots. For this reason, two projection cycles for each capture of three images are adopted in the system. Figure 4 demonstrates the timeline for capturing three images in two projection cycles.

### 3. Advanced Techniques Involved

#### A. Gamma Correction for Nonsinusoidal Error Compensation

Since the 3D shape information is naturally encoded into the patterns projected onto the object surfaces, the full-field fringe information must be extracted in order to reconstruct the 3D points. This can be done by using sinusoidal fringe patterns as well as the phase shifting algorithm. In general, the fringes are straight, evenly spaced, and oriented vertically or horizontally. They are generated in a numerical fashion with the following function:

$$I_i(x, y) = I_0 \left[ 1 + \cos \left( 2\pi k \frac{x}{w} + \delta_i \right) \right], \quad (1)$$

where  $I$  is the intensity value of the pattern at pixel coordinate  $(x, y)$ , the subscript  $i$  denotes the  $i$ th image,  $I_0$  is a constant coefficient indicating the intensity modulation value,  $k$  is the number of fringes in the image,  $w$  is the width of the pattern, and  $\delta$  is the phase shifting amount. Figure 5 shows a few representative fringe patterns.

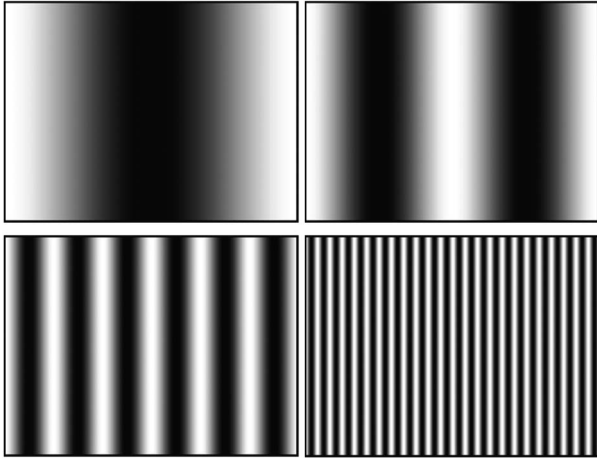


Fig. 5. Projection fringe patterns with 1, 2, 6, and 24 fringes.

To enhance the visual effect of the projected images, the commercial DLP projectors apply gamma modifications to the projection output, which leads to a change in the projected intensity distribution and thus bringing errors to the fringe-pattern intensities. Certain gamma correction can be applied at the camera side when capturing the images, but such a correction is often insufficient. The overall gamma distortion of the encoding projector and the decoding camera pair can be described as

$$I_n = I^{\gamma_0}, \quad (2)$$

where  $I_n$  and  $I$  denote the normalized intensity values of the captured and computer-generated sinusoidal fringe images, and  $\gamma_0$  is the gamma value of the system (typically in the range of 1.8–2.6). To cope with the nonsinusoidal intensity distortion issue, a simple yet effective solution is to modify the initial fringe patterns to compensate for error. This way, Eq. (2) becomes  $I_n = (I^{\frac{1}{\gamma_p}})^{\gamma_0}$ , where  $\gamma_p$  is the pre-encoding factor. Accordingly, Eq. (1) becomes:

$$I = 2I_0 \left[ \frac{1}{2} + \frac{1}{2} \cos \left( 2\pi k \frac{x}{w} + \delta \right) \right]^{\frac{1}{\gamma_p}}, \quad (3)$$

where the value of  $\gamma_p$  can be changed easily during measurement to account for different conditions. It is noted that many existing approaches to gamma correction [16–19] use statistical methods, where the main disadvantage is the complexity of the associated mathematical calculation. The approach used here [20] involves solving the gamma problem at the source before projection, so no extra calculation is required for the measurement system. This scheme helps increase the quality of the fringe patterns while maintaining fast processing speed.

#### B. Multiple-Frequency Fringes for Fast Phase Unwrapping

After capturing the fringe patterns, the next step is to obtain the full-field phase distributions of the fringes. This includes a simple standard

phase-shifting algorithm for the calculation of wrapped phase and a subsequent algorithm for phase unwrapping.

Phase unwrapping is a challenging task in FPP-based 3D imaging and shape measurement when the system deals with multiple separated objects or the object has a complex shape. Although there are numerous existing phase unwrapping methods [21–23], they are not suitable for fringe analysis in fast-speed and high-accuracy 3D imaging. In this work, an efficient and robust approach based on using multiple-frequency fringes are adopted to tackle the problem. As shown in Fig. 5, the technique uses a set of fringe patterns with various frequencies, and the lowest-frequency fringe pattern has only one fringe in it. The one-fringe pattern not only yields phase distributions in a fast manner, but also provides the required integer fringe order offsets for the higher fringe frequencies. The corresponding algorithm can be expressed as

$$\phi_i^{uw}(u, v) = \phi_i^w(u, v) + \text{INT} \left( \frac{\phi_{i-1}^{uw} \frac{f_i}{f_{i-1}} - \phi_i^w}{2\pi} \right) 2\pi, \quad (4)$$

where the subscript  $i$  indicates the  $i$ th projection fringe pattern with  $i = \{2, 3, \dots, n\}$ , and  $n$  is the number of fringe frequencies. In the equation,  $uw$  and  $w$  denote unwrapped phase and wrapped phase, respectively;  $f$  is the number of fringes in the projection pattern, and  $f_n > f_{n-1} > \dots > f_1 = 1$ ; INT represents the rounding function for a decimal number; the wrapped phase  $\phi_i^w$  can be determined from the traditional phase-shifting algorithm. The ratio of two adjacent fringe frequencies  $\frac{f_i}{f_{i-1}}$  is normally smaller than 10 to avoid the noise effect and ensure the reliability of the measurement system.

Due to the simplicity of the governing equation, Eq. (4), the full-field unwrapped phase distributions can be determined in a hyperfast manner. In practice, a variety of phase-shifting steps and fringe frequencies can be employed to satisfy the imaging and measurement requirements. For instance, a set of two fringe frequencies (e.g., 1 and 5) can be combined with the three-step phase-shifting scheme for measuring multiple objects with complex shapes in real time, whereas the widely used four-step phase-shifting scheme with a larger set of fringe frequencies (e.g., a set of four: 1, 4, 20, 100) can help the system better cope with noise and errors to obtain full-field phase distributions with very high accuracy. In the same manner, a single-frequency fringe projection setup can be utilized to achieve very fast 3D imaging with reduced accuracy.

#### C. Phase Correction Scheme for Fast-Speed System

A notable issue with the aforementioned phase-shifting approach comes from the noise effect when the system uses only single or double fringe frequencies for ultrafast-speed measurement. Considering that the multiple-frequency fringes approach can



cope well with the noise issue, the principle of the new approach here is using the accurate unwrapped phase extracted from the multiple-frequency fringes to correct the phase determined from the single- or double-frequency fringe patterns. The procedure of the phase correction is summarized as follows:

1. Capture the first group of images that involve three-step phase-shifting and single- or double-frequency patterns.
2. Capture the second group of images that include three- or larger-step phase-shifting and patterns with a relatively larger number of fringe frequencies (e.g., a set of four: 1, 4, 20, and 100).
3. Match the unwrapped phase distributions from the two cases to generate a phase look-up table (LUT) for the single or double-frequency case.
4. Use the LUT for the future applications that employ three-step phase-shifting and single- or double-frequency patterns for ultrafast-speed measurement.

This phase correction process is of great importance to the proposed system because it will use only single- or double-frequency fringe patterns in order to obtain fast-speed performance. Figure 6 shows an example of phase extraction results before and after using the phase correction scheme.

#### D. System Calibration for an Arbitrary System Setup

The primary task of the FPP-based 3D imaging and shape measurement is to accurately extract the out-of-plane height and depth distributions, from which the in-plane dimensions can be further determined from a simple transformation. The mathematical governing equation of the out-of-plane height or depth determination for a generalized setup where the system components can be arbitrarily positioned is [24]:

$$z = \frac{1 + c_1\phi + (c_2 + c_3\phi)i + (c_4 + c_5\phi)j}{d_0 + d_1\phi + (d_2 + d_3\phi)i + (d_4 + d_5\phi)j}, \quad (5)$$

where  $z$  is the out-of-reference-plane height or depth at pixel  $(i, j)$ ,  $\phi$  is the unwrapped phase determined by Eq. (4), and the coefficients  $c_1 - c_5$  and  $d_0 - d_5$  are constant coefficients determined by geometrical and other system parameters. In the case of

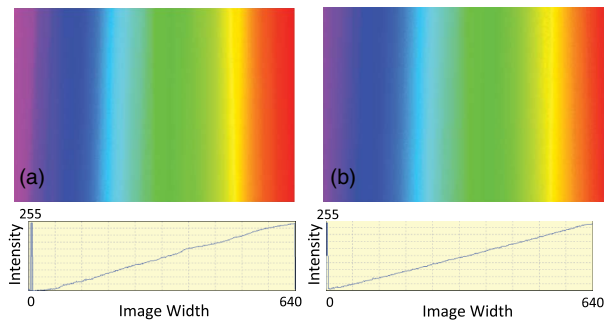


Fig. 6. Phase distribution results before (left) and after (right) error compensation with LUT.

non-negligible lens distortion exists, extra terms of second order of  $i$  and  $j$  can be incorporated into the equation to enhance the 3D imaging accuracy in practice. With this effective scheme, Eq. (5) can be improved as

$$\begin{aligned} z &= \frac{f_c}{f_d} \\ f_c &= 1 + c_1\phi + (c_2 + c_3\phi)i + (c_4 + c_5\phi)j \\ &\quad + (c_6 + c_7\phi)i^2 + (c_8 + c_9\phi)j^2 \\ &\quad + [(c_{10} + c_{11}\phi) + (c_{12} + c_{13}\phi)i \\ &\quad + (c_{14} + c_{15}\phi)j + (c_{16} + c_{17}\phi)ij]ij \\ f_d &= d_0 + d_1\phi + (d_2 + d_3\phi)i + (d_4 + d_5\phi)j \\ &\quad + (d_6 + d_7\phi)i^2 + (d_8 + d_9\phi)j^2 \\ &\quad + [(d_{10} + d_{11}\phi) + (d_{12} + d_{13}\phi)i \\ &\quad + (d_{14} + d_{15}\phi)j + (d_{16} + d_{17}\phi)ij]ij. \end{aligned} \quad (6)$$

The calibration of the system [24–26] can be accomplished by using a number of precise gage blocks of different heights. Such a calibration method can yield high accuracy in 3D object measurements, but it is not very practical for broad applications due to the cost and challenges of manufacturing highly accurate and precise gage blocks with various sizes. In this paper, a flexible calibration technique that uses a checker or concentric-circle pattern board as a flexible gage object is employed [27,28].

The flexible FPP calibration technique requires capturing a series of fringe patterns projected on the planar calibration board with different positions (e.g., 10–20 positions). By averaging the captured fringe images, high definition calibration board images can be created for a bundle-adjustment-based camera calibration process [29] to obtain the intrinsic and extrinsic parameters of the camera as well as the 3D coordinates of each control point on the calibration board with hyperhigh accuracy. These control points can then serve as gage points to calibrate the FPP-based 3D imaging system using a nonlinear least-squares approach as follows:

$$S = \sum_{n=1}^i \sum_{k=1}^j \left( \frac{f_c}{f_d} - Z_{nk} \right)^2, \quad (7)$$

where  $Z_{nk}$  is the height or depth information of  $k$ th control point on the calibration board obtained at the  $n$ th calibration position. The constant coefficients  $c_1 - c_{17}$  and  $d_0 - d_{17}$  in the governing Eq. (6) can be determined by using the well-known Levenberg–Marquardt (L-M) algorithm. The initial guess of the coefficients is obtained by minimizing a linear least-squares cost function of  $S' = \sum_{n=1}^i \sum_{k=1}^j (f_c - f_d Z_{nk})^2$ . The complication of the above governing equations and the system calibration process require at least three different positions of the calibration board to reliably determine the

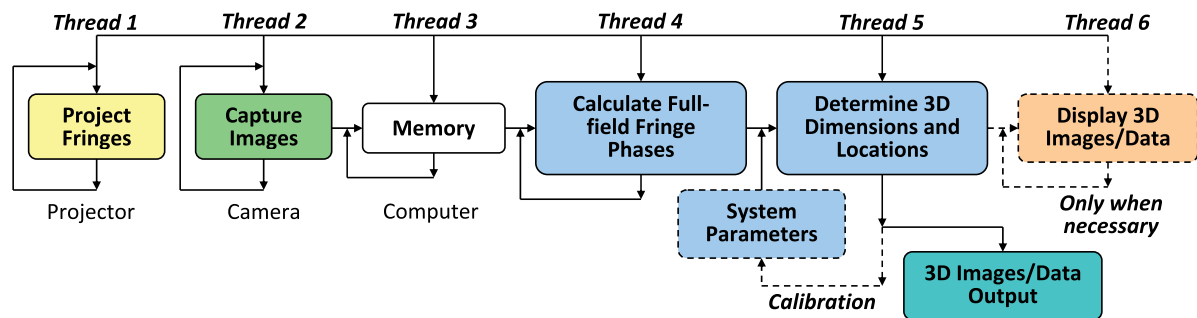


Fig. 7. Flowchart of the proposed 3D imaging system.

coefficients. More positions usually lead to more accurate calibration, but further improvement is negligible for a total position number larger than 20.

#### E. Multithread Computing for Projecting, Capturing, and Processing

To achieve fast speed and high accuracy 3D imaging, the system uses multithread computing for projecting, capturing, and processing. Figure 7 illustrates a flowchart of the proposed 3D imaging system. It is evident that the subtasks are separated into multithread in a parallel mode, which helps maintain a real-time speed for highly accurate 3D imaging.

#### F. Using CUDA and OpenGL for Enhanced Performance

As previously mentioned, multiple-frequency fringes can be used to enhance the imaging and measurement accuracy. Because the fringe patterns for projection need to be changed periodically, the pattern changing can cause system instability and production of incorrect 3D results at a high rate of projecting and capturing. The problem comes from the instability in the time of process of transferring data from the random-access memory (RAM) of the computer to the memory of the GPU. Figure 8 shows the relation between the computer as a host and the GPU. Since the patterns are generated by the central processing unit (CPU) and stored in RAM, every time a new pattern needs to be displayed, the CPU will transfer the pattern data from host memory to the global memory of the GPU device. The time required for such data transaction is not a constant, and it can vary from 10 to 200 ms. This instability prevents the system from producing 3D imaging results accurately and with stability.

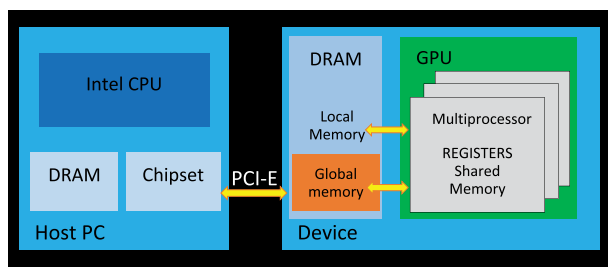


Fig. 8. Relation between the computer host and the graphical device.

The display instability problem can be well resolved by the implementation of CUDA (an acronym for Compute Unified Device Architecture) programming. CUDA is a parallel computing architecture developed by NVIDIA, and it allows programs to access the memory of the graphical device and take advantage of the GPU to process data. By using CUDA, the entire process of projection, including generating data and displaying it on the screen, can be done solely within the GPU. Therefore, no data transaction or communication is needed between the host and the graphical device. In addition, because of its natural functionality, the graphical device is able to handle the switching of patterns in a very stable manner.

In order to display the patterns provided by the GPU and CUDA, OpenGL (Open Graphics Library)

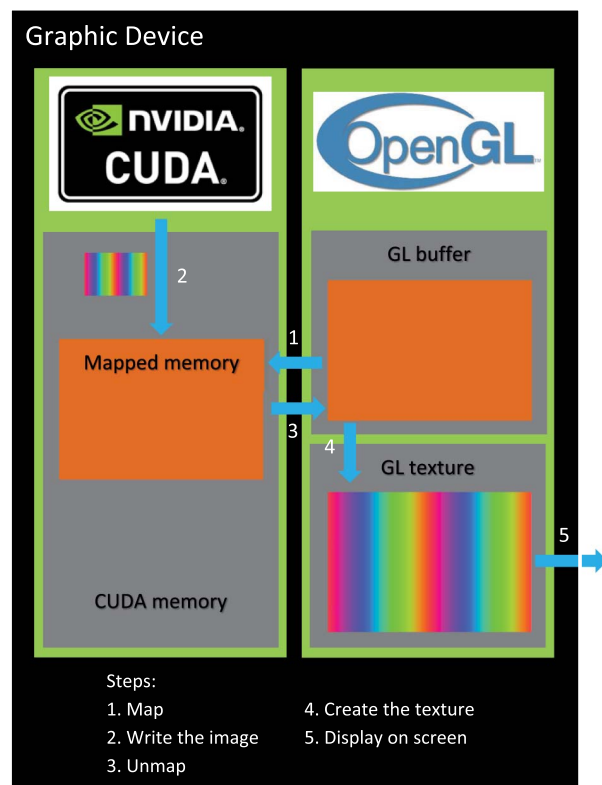


Fig. 9. CUDA and OpenGL interoperation for generating and displaying patterns.

is also needed for the purpose of fast and reliable display. OpenGL is a software interface to the graphic device, and is used to draw pixel or vertices on the screen. By using the OpenGL interoperability with CUDA, the pattern generated by the CUDA part is shown on screen or projected on scene very rapidly because they share data through the common memory in the frame buffer. Figure 9 illustrates the interoperation of CUDA and OpenGL to generate and display patterns with the GPU.

#### 4. Experiments

In order to demonstrate the validity and applicability of the described system, some evaluation experiments have been carried out and are presented here. In the experiments, the camera and projector are arbitrarily positioned to form a generalized setup. The distances among the camera, the projector, and the virtual reference plane as well as the size of the field of view are adjusted according to the object sizes in each experiment.

##### A. Accuracy Test

In the accuracy test, two different fringe frequencies, with 1 and 5 fringes in the projection images, respectively, combined with the three-step phase-shifting algorithm were used in the experiment. A cubic gage block of side length 101.60 mm is placed at a few different locations in the field of view (411.0 mm wide) to determine the accuracy of the system. The measurement indicates that the average height of the gage block is 101.64 mm with a standard deviation of 0.07 mm, where the average and standard deviation are calculated from the points on the surface of the block at all those locations. Thus the relative accuracy can be calculated from the ratio of the measurement error to the width of the measurement field as  $(101.64 - 101.6 \text{ mm})/411.0 \text{ mm} \approx 0.01\%$ . This high accuracy is very important for many applications such as product inspection, reverse engineering, and quality control.

##### B. Multiple Objects Test

The second experiment was conducted to simultaneously measure the 3D shapes of multiple objects which are shown in Fig. 10 along with the results in 2D and 3D plots. This experiment demonstrates the effectiveness of the direct phase unwrapping with double-frequency fringes. When using a conventional phase unwrapping scheme instead of the adopted one, it takes a long time to obtain a correct full-field unwrapped phase map for the fringe image, because identifying the fringe-order-offsets in each separate region relies on a time-consuming and ambiguous manual analysis.

##### C. Speed Test

In the experiments, the refresh rate of the projector was set to 90 Hz and the resolution of the camera was set to 640 pixels by 480 pixels to utilize its high speed. When using a single fringe frequency in the measurement, the 3D images were successfully

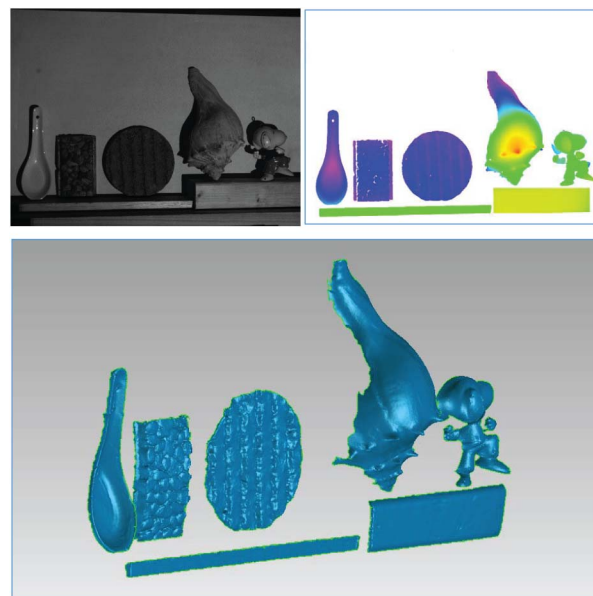


Fig. 10. 3D shape measurement of multiple objects with complex shapes.

reconstructed at a speed of 45 fps. As described earlier, it takes two projection cycles to capture three images, and that is why 45 fps instead of 90 fps was achieved. Although the imaging accuracy at this speed is relatively lower (about 0.04% relative accuracy), the case can be very useful for applications where imaging speed has a higher priority than imaging accuracy. Experiments also show that when double-frequency fringe projection is adopted, the six images captured in four projection cycles can help archive 3D imaging and shape measurement at speed of 22.5 fps with enhanced accuracy of 0.01% (as previously described).

#### 5. 360° 3D Model Generation

To demonstrate the practicability and reliability of the FPP-based approach for 3D imaging and shape reconstruction of objects with complex shapes, the proposed system has also been employed to reconstruct the complete 360° 3D images of a few other samples with different surface roughnesses and surface colors. In each experiment, eight different 3D views were acquired first; they are then stitched together to form a complete 360° 3D image. The 3D stitching process mainly comprises a data registration step to align the multiple 3D views and a remeshing step to merge them together and discard redundant overlapping regions. Figure 11 shows the corresponding results where the first image in each row was captured by a conventional digital camera and the other images were selected views of the 3D model reconstructed by the 3D imaging system. A direct visual inspection verifies that the 3D images have a very good match with the physical objects.



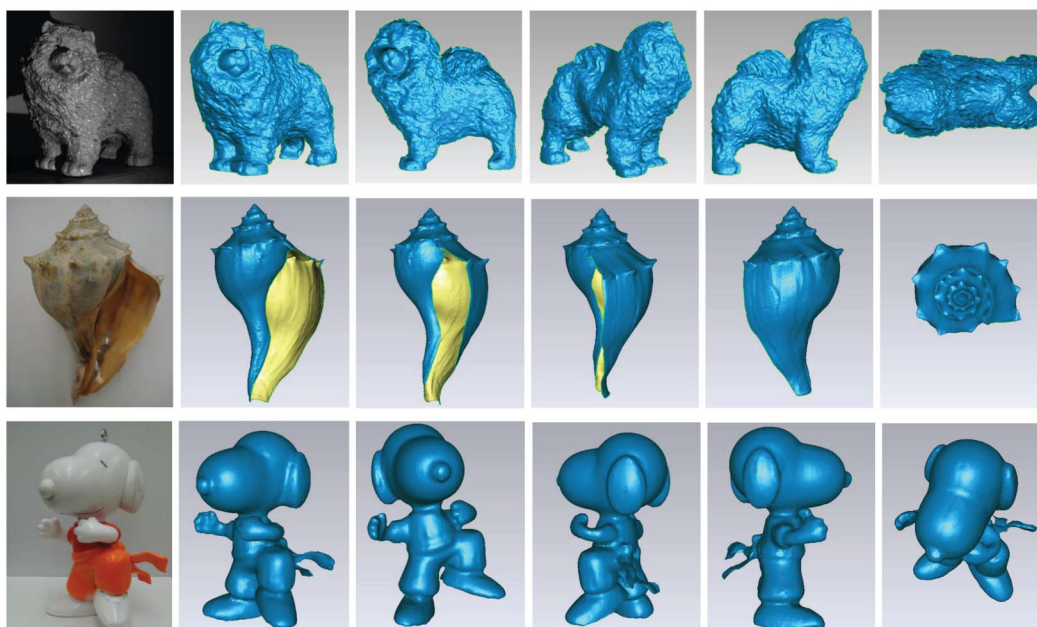


Fig. 11. 360° reconstructed models of three objects.

## 6. Conclusion

This paper has presented a real-time and high-accuracy 3D imaging and shape measurement system based on fringe projection profilometry and phase-shifting technique. By integrating three gray-scale phase-shifted fringe patterns into a single color image and using an external triggering circuit to synchronize the projector and the camera as well as employing a series of advanced approaches to cope with various uncertainties and errors, the system is capable of performing 3D imaging and shape measurement of multiple objects with complex shapes at fast speed with high accuracy. The real-time system can reach a speed of 45 fps with relative accuracy of 0.04% and a slower speed of 22.5 fps with enhanced accuracy of 0.01%.

It should be pointed out that the adoption of 90 Hz projection rate and the corresponding 22.5 or 45 fps measurement speed are limited by the processing capacity of the computer program developed in this work. Technically, a faster measurement speed can be obtained by using a higher projection rate (such as 120 Hz) if the projector, the camera, and the processing program can handle such a speed. In the case of this work, the processing program cannot cope with the 120 Hz rate unless the image resolution is reduced to 320 pixels by 240 pixels, which is too low to use. Nevertheless, to achieve a substantially faster speed with unaltered accuracy is technically feasible with high-performance system components.

In recent years, there have been high demands for the 3D imaging and shape measurement techniques to possess a number of advanced technical features such as fast speed and high accuracy. The system presented in this paper has demonstrated the capability of satisfying these demands. It also shows promise for helping develop future 3D imaging and

shape measurement systems with unprecedented performance.

## References

1. F. Chen, G. Brown, and M. Song, "Overview of three-dimensional shape measurement using optical methods," *Opt. Eng.* **39**, 10–22 (2000).
2. J. Burke, T. Bothe, W. Osten, and C. Hess, "Reverse engineering by fringe projection," *Proc. SPIE* **4778**, 312–324 (2002).
3. F. Blais, "Review of 20 years of range sensor development," *J. Electron. Imaging* **13**, 231–243 (2004).
4. S. C. Park and M. Chang, "Reverse engineering with a structured light system," *Comput. Ind. Eng.* **57**, 1377–1384 (2009).
5. D. Hong, H. Lee, M. Kim, H. Cho, and J. Moon, "Sensor fusion of phase measuring profilometry and stereo vision for three-dimensional inspection of electronic components assembled on printed circuit boards," *Appl. Opt.* **48**, 4158–4169 (2009).
6. J. Geng, "Structured-light 3D surface imaging: a tutorial," *Adv. Opt. Photon.* **3**, 128–160 (2011).
7. S. Zhang and P. S. Huang, "High-resolution, real-time three-dimensional shape measurement," *Opt. Eng.* **45**, 123601 (2006).
8. C. Zuo, Q. Chen, G. Gu, S. Feng, and F. Feng, "High-speed three-dimensional profilometry for multiple objects with complex shapes," *Opt. Express* **20**, 19493–19510 (2012).
9. K. Liu, Y. Wang, D. Lau, Q. Hao, and L. Hassebrook, "Dual-frequency pattern scheme for high-speed 3-D shape measurement," *Opt. Express* **18**, 5229–5244 (2010).
10. Z. Wang, H. Du, S. Park, and H. Xie, "Three-dimensional shape measurement with a fast and accurate approach," *Appl. Opt.* **48**, 1052–1061 (2009).
11. S. S. Gorthi and P. Rastogi, "Fringe projection techniques: whither we are?" *Opt. Lasers Eng.* **48**, 133–140 (2010).
12. J. Salvi, S. Fernandez, T. Pribanic, and X. Llado, "A state of the art in structured light patterns for surface profilometry," *Pattern Recognition* **43**, 2666–2680 (2010).
13. X. Su and Q. Zhang, "Dynamic 3-D shape measurement method: a review," *Opt. Lasers Eng.* **48**, 191–204 (2010).
14. Y. Fu and Q. Luo, "Fringe projection profilometry based on a novel phase shift method," *Opt. Express* **19**, 21739–21747 (2011).
15. B. Li, N. Karpinsky, and S. Zhang, "Novel calibration method for structured-light system with an out-of-focus projector," *Appl. Opt.* **53**, 3415–3426 (2014).



16. B. Pan, Q. Kemao, L. Huang, and A. Asundi, "Phase error analysis and compensation for nonsinusoidal waveforms in phase-shifting digital fringe projection profilometry," *Opt. Lett.* **34**, 416–418 (2009).
17. Z. Li, Y. Shi, C. Wang, and Y. Wang, "Accurate calibration method for a structured light system," *Opt. Eng.* **47**, 053604 (2008).
18. S. Zhang and S. Yau, "Generic nonsinusoidal phase error correction for three-dimensional shape measurement using a digital video projector," *Appl. Opt.* **46**, 36–43 (2007).
19. S. Ma, C. Quan, R. Zhu, L. Chen, B. Li, and C. J. Tay, "A fast and accurate gamma correction based on Fourier spectrum analysis for digital fringe projection profilometry," *Opt. Commun.* **285**, 533–538 (2012).
20. T. Hoang, B. Pan, D. Nguyen, and Z. Wang, "Generic gamma correction for accuracy enhancement in fringe-projection profilometry," *Opt. Lett.* **35**, 1992–1994 (2010).
21. L. Kinell, "Spatiotemporal approach for real-time absolute phase measurements by use of projected fringes," *Appl. Opt.* **43**, 3018–3027 (2004).
22. J. Tian and X. Peng, "Three-dimensional vision from a multi-sensing mechanism," *Appl. Opt.* **45**, 3003–3008 (2006).
23. W. Osten and P. Ferraro, "Digital holography and its application in MEMS/MOEMS inspection," in *Optical Inspection of Microsystems*, W. Osten, ed. (CRC, 2006), 351–425.
24. H. Du and Z. Wang, "Three-dimensional shape measurement with an arbitrarily arranged fringe projection profilometry system," *Opt. Lett.* **32**, 2438–2440 (2007).
25. Z. Wang, D. Nguyen, and J. Barnes, "Some practical considerations in fringe projection profilometry," *Opt. Lasers Eng.* **48**, 218–225 (2010).
26. L. Huang, P. Chua, and A. Asundi, "Least-squares calibration method for fringe projection profilometry considering camera lens distortion," *Appl. Opt.* **49**, 1539–1548 (2010).
27. M. Vo, Z. Wang, T. Hoang, and D. Nguyen, "Flexible calibration technique for fringe-projection-based three-dimensional imaging," *Opt. Lett.* **35**, 3192–3194 (2010).
28. M. Vo, Z. Wang, B. Pan, and T. Pan, "Hyper-accurate flexible calibration technique for fringe-projection-based three-dimensional imaging," *Opt. Express* **20**, 16926–16941 (2012).
29. M. Vo, Z. Wang, L. Luu, and J. Ma, "Advanced geometric camera calibration for machine vision," *Opt. Eng.* **50**, 110503 (2011).